Scalable Coupling Emulation for Active Antenna Arrays Under Load Modulation

Citation for the original published paper (version of record):
Fernandez, J., Buisman, K., Anttila, L. et al (2026). Scalable Coupling Emulation for Active Antenna Arrays Under Load Modulation. IEEE Microwave and Wireless Technology Letters, 36(7): 1216-1219. http://dx.doi.org/10.1109/LMWT.2026.3668420

Scalable Coupling Emulation for Active Antenna Arrays Under Load Modulation

Joel Fernandez, *Student Member, IEEE*, Koen Buisman, *Senior Member, IEEE*, Lauri Anttila, *Member, IEEE*, Christian Fager, *Fellow, IEEE*, Thomas Eriksson, *Senior Member, IEEE*, and Mikko Valkama, *Fellow, IEEE*

***Abstract*—This letter addresses measurement-based coupling emulation of power amplifier (PA) arrays with more than four elements, enabling scalable characterization of multiantenna transmitters (TXs). A refined estimation procedure for driver gain is proposed, improving the convergence stability and accuracy over prior methods, while also addressing the estimation of the involved load reflection coefficients. Measurements with up to 16-PA arrays demonstrate reliable error convergence and accurate *S*-parameter recovery, while we also confirm the anti-symmetric variation of the load reflection coefficient with beamforming angle. The results show a reduced branch-to-branch injection-error variance compared to prior art methods, further supporting the scalability of the proposed estimator. Furthermore, combined far-field adjacent-channel power ratio (ACPR) and error vector magnitude (EVM) metrics for a phased-array TX exhibit the expected symmetry versus beam angle and reveal direction-dependent nonlinearity, validating realistic array-level radiated performance after spatial combining. Notably, this work also integrates a 5G-NR compliant waveform for the first time in a coupling-emulation framework, paving the way for efficient modeling and linearization of next-generation wireless TXs under load modulation.**

***Index Terms*—5G, 6G, active array transmitters (TXs), coupling emulation, load modulation, load pulling, power amplifier (PA).**

I. Introduction

ENHANCING sustainability and energy efficiency is a key objective as wireless networks evolve toward 6G [1], [2]. Transmitter (TX) power amplifiers (PAs) account for a significant share of total power consumption, making accurate modeling and optimization essential for energy-efficient massive MIMO and beamforming systems [3], [4]. Traditional approaches, such as transistor-level modeling and load–pull techniques [5], [6], allow rapid design exploration but fail to capture nonlinear effects such as trapping and memory phenomena, particularly under broadband or modulated signals [7].

Received 16 January 2026; revised 19 February 2026; accepted 21 February 2026. Date of publication 4 March 2026; date of current version 8 July 2026. This work was supported in part by the Research Council of Finland under Grant 367800 and in part by Business Finland under the RF ECO3 and MULTIRACS Projects. *(Corresponding author: Joel Fernandez.)*

Joel Fernandez, Lauri Anttila, and Mikko Valkama are with Tampere University, 33014 Tampere, Finland (e-mail: joel.fernandez@tuni.fi).

Koen Buisman is with the University of Surrey, GU2 7XH Guildford, U.K., and also with the Chalmers University of Technology, 412 96 Gothenburg, Sweden.

Christian Fager and Thomas Eriksson are with the Chalmers University of Technology, 412 96 Gothenburg, Sweden.

Digital Object Identifier 10.1109/LMWT.2026.3668420

Measurement-based emulation frameworks address these limitations. The active load–pull method in [8] introduced PA coupling emulation, but validation was limited to three-element arrays and narrowband signals. Successful emulation was later demonstrated for Doherty architectures in [9], being, however, constrained to two-element setups only while also lacking detailed convergence analysis and wideband, 5G-NR-compliant signals. More recently, Mengozzi et al. [10] demonstrated emulation for a 2×2 active array with modulated signals (four elements in total), further extending validation. In parallel, FIR-based least-square (LS) estimation was proposed in [11], but applied only to reflection/transmission coefficient extraction in active load-pull, without extension to full array emulation or driver-gain estimation. Recent advances in load-modulation-aware modeling [12] and linearization [13] further underline the need for accurate coupling emulation in 5G and beyond.

In this work, we extend the prior emulation framework of [8] and [9] with several key contributions. First, we experimentally demonstrate, for the first time, coupling emulation in arrays with more than four elements, enabling scalable modeling of larger multiantenna systems. Second, we introduce an enhanced procedure for estimating the driver gain, improving convergence stability and accuracy; a similar approach is also applied to load-reflection coefficient estimation. Third, we demonstrate error convergence and *S*-parameter recovery for an eight-PA configuration, together with complementary 16-PA results showing reduced branch-to-branch injection-error spread, thus supporting improved scalability of the proposed estimator framework. Fourth, we compare our estimates of the driver gain and load reflection coefficient with earlier FFT-based methods, showing improved consistency and reliability. Fifth, we validate the anti-symmetric behavior of the load reflection coefficient versus beamforming angle in a four-PA setup, supported by per-PA adjacent-channel power ratio (ACPR) as well as far-field ACPR and error vector magnitude (EVM) measurements, confirming physically consistent array-level behavior. Notably, this is the first demonstration of coupling emulation using a 5G-NR compliant wideband waveform, offering a robust and scalable platform for accurate modeling and linearization of complex multiantenna TXs in next-generation wireless networks.

II. Methods

The coupling-emulation framework builds on the iterative measurement-based method proposed in [8] and [9],

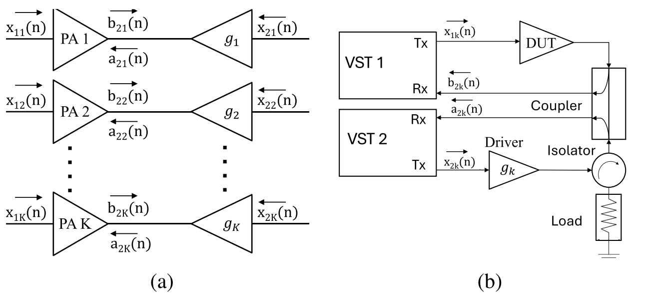

Fig. 1. (a) Conceptual block diagram of the emulated PA array, representing the effective coupled behavior achieved through the emulation process. (b) Simplified block diagram of the actual measurement setup used to realize and characterize the emulated array in (a).

enabling accurate reproduction of mutual coupling effects in active antenna arrays using a single device-under-test (DUT). Fig. 1(a) illustrates a conceptual K-element array with primary inputs x_{1k}, outputs b_{2k}, reflected waves a_{2k}, and secondary injections x_{2k}, where the subscripts 1, 2 follow two-port network notation while the subscript k identifies the kth PA branch. Fig. 1(b) shows the actual measurement setup to emulate the PA array in Fig. 1(a). Throughout this section, $n = 0, 1, \ldots, N-1$ denotes the discrete-time sample index for a segment of N samples. The superscript i represents the current iteration of the emulation.

When properly designed and deployed, the emulation iteratively converges toward steady-state coupled behavior without requiring physical construction of the full system. During each iteration i, the DUT is sequentially excited to emulate the output of each array element, with a fixed primary excitation x_{1k} and an iteratively updated secondary injection x_{2k}; hence, the DUT input power remains constant and output-power variations across iterations are small and do not affect convergence.

A. Iterative Emulation Algorithm

At initialization ($i = 0$), the secondary input signals are set to $x_{2k}^{(0)}[n] = 0$ for all k, assuming isolated PAs. For iteration $i \geq 1$, assuming frequency-flat coupling, the desired incident wave at branch k is updated as

$$a_{2k,\text{desired}}^{(i)}[n] = \sum_{j=1}^{K} S_{kj} b_{2j}^{(i-1)}[n] \tag{1}$$

where S_{kj} is the complex coupling coefficient from branch j to branch k. The secondary injection is then updated in the frequency domain as $X_{2k}^{(i)}[f] = A_{2k,\text{desired}}^{(i)}[f]/\hat{G}_k^{(i)}[f]$, where $X_{2k}^{(i)}[f]$ and $A_{2k,\text{desired}}^{(i)}[f]$ are the Fourier transforms of the corresponding time-domain signals, and $\hat{G}_k^{(i)}[f]$ is the Fourier transform of the driver-gain estimate (4) from Section II-B. $X_{2k}^{(i)}[f]$ is then converted to time domain, and applied to the DUT along with $x_{1k}^{(i)}[n]$, after which the measured $a_{2k}^{(i)}[n]$ and $b_{2k}^{(i)}[n]$ are recorded for the next iteration. We note that despite the frequency-flat coupling model assumed here, the framework itself can be generalized to frequency-dependent coupling via extending (1) to a time-domain convolutional model.

Convergence at iteration i is monitored using two normalized mean squared-error (NMSE) metrics. The iteration *stability metric* is $\text{NMSE}_1^{(i,k)} = \|a_{2k,\text{desired}}^{(i)} - a_{2k,\text{desired}}^{(i-1)}\|^2/\|a_{2k,\text{desired}}^{(i)}\|^2$, and the injection *accuracy metric* is $\text{NMSE}_2^{(i,k)} = \|a_{2k,\text{desired}}^{(i)} - a_{2k}^{(i)}\|^2/\|a_{2k,\text{desired}}^{(i)}\|^2$. Iterations continue until both metrics reach a converged state.

B. Proposed Convolution-Based Driver Gain Estimation

To capture the dynamic memory effects within the iterative procedure in Section II-A, the gain of the driver (assumed predominantly linear) for branch k at iteration i is modeled as an FIR filter of length M_g taps, where the driver and DUT are dimensioned such that the driver operates well within its linear region. The time-domain model is thus of the form

$$a_{2k}^{(i)}[n] = \sum_{m=0}^{M_g-1} g_k^{(i)}[m]\, x_{2k}^{(i)}[n-m] + e_k^{(i)}[n] \tag{2}$$

where $g_k^{(i)}[m]$ are the filter taps and $e_k^{(i)}[n]$ is the residual. In matrix form, this can be expressed as

$$\mathbf{a}_{2k}^{(i)} = \mathbf{X}_{2k}^{(i)} \mathbf{g}_k^{(i)} + \mathbf{e}_k^{(i)} \tag{3}$$

with $\mathbf{a}_{2k}^{(i)} = [a_{2k}^{(i)}[0], \ldots, a_{2k}^{(i)}[N-1]]^{\mathsf{T}}$, $\mathbf{g}_k^{(i)} = [g_k^{(i)}[0], \ldots, g_k^{(i)}[M_g - 1]]^{\mathsf{T}}$, $\mathbf{e}_k^{(i)} = [e_k^{(i)}[0], \ldots, e_k^{(i)}[N-1]]^{\mathsf{T}}$, and $\mathbf{X}_{2k}^{(i)}$ is the $N \times M_g$ (Toeplitz) convolution matrix constructed from time-shifted samples of $x_{2k}^{(i)}[n]$. The LS estimate can then be written as

$$\hat{\mathbf{g}}_k^{(i)} = \left(\mathbf{X}_{2k}^{(i)H} \mathbf{X}_{2k}^{(i)}\right)^{-1} \mathbf{X}_{2k}^{(i)H} \mathbf{a}_{2k}^{(i)}. \tag{4}$$

This LS-based estimation is more stable and accurate than the FFT-based methods used in [8] and [9]. And more importantly, the improved numerical conditioning is critical for scalability: as the array size grows and coupling levels span a wider dynamic range, bin-wise FFT ratios become increasingly ill-conditioned. The proposed LS-based convolutional estimator removes this bottleneck and thereby enables reliable extension of coupling emulation beyond small arrays.

C. Proposed Load Reflection Coefficient Estimation

To assess and estimate the load reflection coefficient, especially in the phased-array context, we propose to model it as an FIR filter of length M_Γ. In the time domain, for branch k at iteration i, the reflected wave satisfies $b_{2k}^{(i)}[n] = \sum_{m=0}^{M_\Gamma - 1} h_k^{(i)}[m]\, a_{2k}^{(i)}[n-m] + v_k^{(i)}[n]$, where $h_k^{(i)}[m]$ are the FIR taps and $v_k^{(i)}[n]$ denotes the residual. Using a matrix formulation identical to that in Section II-B, this relation can be written compactly as $\mathbf{b}_{2k}^{(i)} = \mathbf{A}_{2k}^{(i)} \mathbf{\Gamma}_{L,k}^{(i)} + \mathbf{v}_k^{(i)}$, where $\mathbf{\Gamma}_{L,k}^{(i)}$ collects the FIR taps and $\mathbf{A}_{2k}^{(i)}$ is the corresponding convolution matrix formed from time-shifted samples of $a_{2k}^{(i)}[n]$, constructed in the same manner as $\mathbf{X}_{2k}^{(i)}$ in (3). The load-reflection estimate then follows directly from a LSs solution, as $\hat{\mathbf{\Gamma}}_{L,k}^{(i)} = (\mathbf{A}_{2k}^{(i)H} \mathbf{A}_{2k}^{(i)})^{-1} \mathbf{A}_{2k}^{(i)H} \mathbf{b}_{2k}^{(i)}$.

We note that this estimation is independent of the coupling emulation process.

III. RF Measurements

All measurements are conducted on the RF WebLab platform [14], assuming a $K \times 1$ phased-array TX with $\lambda/2$ spacing. The setup uses NI PXIe-5646R/5645R vector signal transceivers (VSTs) at 2.14 GHz to generate excitation

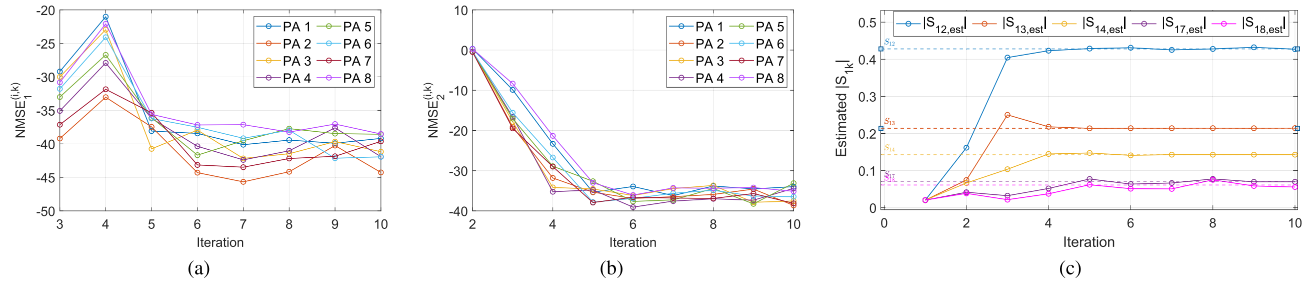

Fig. 2. Convergence of error metrics for the 8-PA case at beamforming angle $\theta = 0°$. (a) $\mathrm{NMSE}_1^{(i,k)}$ for iteration stability. (b) $\mathrm{NMSE}_2^{(i,k)}$ for injection accuracy. (c) Magnitude of the estimated coupling coefficients $|S_{kj,\mathrm{est}}|$, showing successful S-parameter recovery.

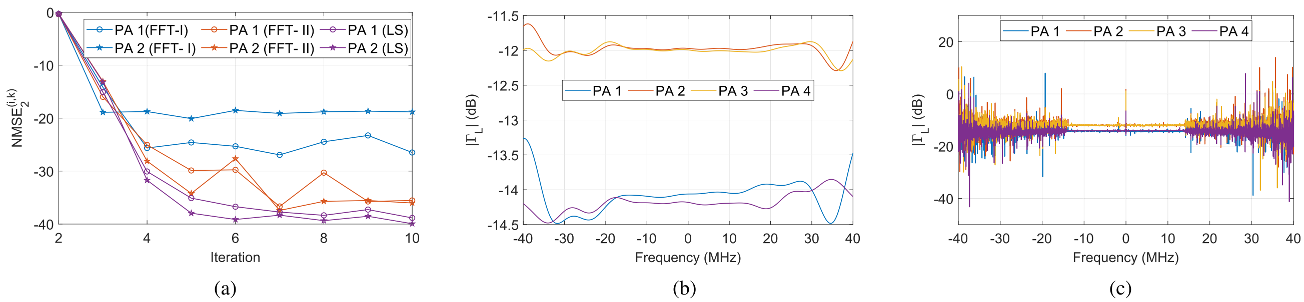

Fig. 3. Comparison of estimation methods at beamforming angle $\theta = 0°$ with $M_g = 5$ (driver gain) and $M_\Gamma = 10$ (load reflection). (a) $\mathrm{NMSE}_2^{(i,k)}$ convergence with the proposed LS-based driver gain estimation versus the two FFT-based variants, FFT-I (single averaged gain) and FFT-II (bin-wise division with selective averaging of outliers) for $K = 2$. (b) Proposed LS-based estimate of $|\Gamma_L|$ for $K = 4$. (c) FFT-based estimate of $|\Gamma_L|$ for $K = 4$.

and apply controlled load modulation. Broadband, essentially linear driver amplifiers with isolators protect the chain, and directional couplers enable calibrated wave measurements. The DUT is a 6-W GaN PA (CGH40006TB) on a standard test board, with calibration performed using short/open/load standards and power-meter alignment at the DUT connectors. Unless otherwise stated, the emulation runs for $N_{\mathrm{iter}} = 10$, and the PA array size is varied as $K \in \{2, 4, 8, 16\}$. The excitation is a 5G-NR-compliant OFDM waveform [30-MHz modulation bandwidth, 30-kHz subcarrier spacing (SCS)] with oversampling and windowing. In all results, we use $M_g = 5$ taps for driver-gain estimation (Section II-B) and $M_\Gamma = 10$ taps for load-reflection estimation (Section II-C). Further platform and calibration details are as in [8], [9], and [14].

To emulate antenna coupling, we adopt a geometric distance-based model [12], [13], [15], where the nearest-neighbor S-parameter [e.g., $|S_{12}| = 0.42$ in Fig. 2(c)] corresponds to about -7.5 dB, representing strong adjacent-antenna interaction. All errors and estimates are evaluated over $3\times$ signal bandwidth (90 MHz) to ensure sufficient dynamic range and capture adjacent channel regions. We first assess scalability for $K = 8$ under a matched-array assumption for S-parameter verification. Fig. 2 shows iteration stability $\mathrm{NMSE}_1^{(i,k)}$ [Fig. 2(a)] and injection accuracy $\mathrm{NMSE}_2^{(i,k)}$ [Fig. 2(b)], both of which decay and stabilize, confirming reliable convergence. In Fig. 2(c), the magnitudes of selected estimated S-parameters are shown. The recovery is highly accurate for $|S_{12,\mathrm{est}}|$, $|S_{13,\mathrm{est}}|$, and $|S_{14,\mathrm{est}}|$, while $|S_{17,\mathrm{est}}|$ and $|S_{18,\mathrm{est}}|$ deviate slightly due to their very low values being more noise-sensitive. These results thus well confirm the scalability of the framework to larger arrays.

We next evaluate the proposed LS-based convolutional driver-gain estimation with $K = 2$. The conventional FFT approach diverges at certain bins unless averaging is applied, so two variants are tested. FFT-I uses a single averaged gain, while FFT-II applies bin-wise division with selective averaging of outliers. As shown in Fig. 3(a), FFT-II is more stable than FFT-I, but both converge more slowly and less smoothly. In contrast, the proposed time-domain LS method converges faster and more consistently, showing greater robustness to memory effects and wideband excitations with fewer iterations.

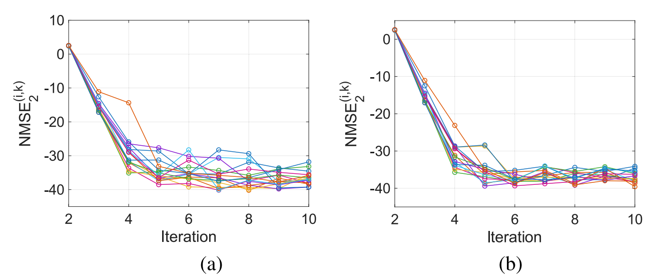

Fig. 4. Injection accuracy $\mathrm{NMSE}_2^{(i,k)}$ across PA branches for the case with $K = 16$ PAs. (a) FFT-II shows a larger performance spread. (b) Proposed LS shows stable performance and lower steady-state variance.

For $K = 4$, Fig. 3(b) shows the proposed LS-based estimate of $|\Gamma_L|$, which is noticeably smoother across frequency compared to the FFT-based frequency-bin division estimate in Fig. 3(c). The LS approach avoids the noise amplification observed in the FFT method, producing stable load trajectories. To further illustrate scalability, Fig. 4 compares FFT-II and LS-based driver-gain estimation for $K = 16$ using the injection-accuracy metric $\mathrm{NMSE}_2^{(i,k)}$ as defined in Section II-A. While the best-branch accuracies are similar, FFT-II exhibits a much larger error variance across branches, whereas the proposed LS approach remains stable and uniform, highlighting its importance for reliable extension of coupling emulation to larger PA arrays.

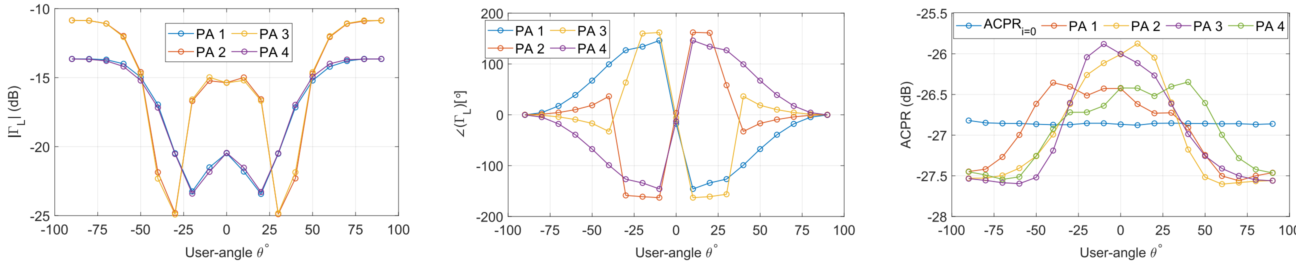

(a) (b) (c)

Fig. 5. Results for the $K = 4$ case as a function of beamforming angle θ. (a) Average $|\Gamma_L|$, exhibiting symmetric behavior. (b) Average $\angle\Gamma_L$, exhibiting anti-symmetric behavior. (c) ACPR versus θ, exhibiting anti-symmetric behavior across user angles. Here, $\text{ACPR}_{i=0}$ denotes the ACPR prior to emulation.

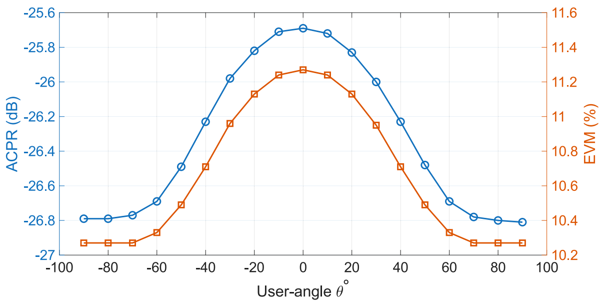

Fig. 6. Far-field ACPR (dB) and EVM (%) versus user angle θ for the $K = 4$ case.

Finally, the spatial behavior of the four-PA array is assessed as a function of the beamforming angle θ, with the spatial combining performed numerically. Fig. 5 shows that the average LS-estimate of $|\Gamma_L|$ [Fig. 5(a)] is symmetric, while that of $\angle\Gamma_L$ [Fig. 5(b)] is anti-symmetric with respect to θ, as expected for a uniform linear array of identical PAs under reciprocal coupling. This anti-symmetry propagates to the ACPR trends [Fig. 5(c)], resulting in anti-symmetric nonlinear distortion across beamforming directions. For reference, the baseline $\text{ACPR}_{i=0}$ prior to emulation remains constant, as expected, across user angles at −26.8 dB. In addition to per-PA results, Fig. 6 shows the spatially combined far-field ACPR and EVM versus user angle θ for the $K = 4$ array. Both metrics exhibit the expected symmetric behavior with respect to θ, consistent with array reciprocity and symmetric load-modulation patterns. At the same time, a clear direction-dependent nonlinearity is observed, with the worst ACPR/EVM near broadside and progressively improved performance at larger scan angles. This confirms that the proposed coupling-emulation framework yields not only physically consistent branch-level behavior but also realistic array-level radiated performance after spatial combining. These spatial patterns further validate that the proposed emulation framework accurately reproduces the physical load modulation dynamics and nonlinear interactions in multiantenna configurations.

IV. Conclusion

This letter presents an enhanced PA array emulation framework that scales existing measurement techniques to larger antenna arrays while incorporating 5G-NR signals for realistic evaluations. The proposed LS-based estimation of driver gain and load reflection coefficients improves convergence stability and accuracy over previously published methods. Experimental results with up to 16-PA configurations confirm reliable error convergence with reduced branch-to-branch injection-error variance and thus improved scalability, accurate S-parameter recovery, while far-field ACPR and EVM metrics confirm physically consistent array-level behavior. Future work will aim to extend the framework to frequency-dependent and more physically detailed coupling models in large PA arrays.

References

[1] *Framework and Overall Objectives of the Future Development of IMT for 2030 and Beyond*, document M.2160-0, Nov.2023.
[2] H.Tataria, M.Shafi, A. F.Molisch, M.Dohler, H.Sjöland, and F.Tufvesson, “6G wireless systems: Vision, requirements, challenges, insights, and opportunities,” *Proc. IEEE*, vol. 109, no. 7, pp. 1166–1199, Jul.2021.
[3] C.Fager, T.Eriksson, F.Barradas, K.Hausmair, T.Cunha, and J. C.Pedro, “Linearity and efficiency in 5G transmitters: New techniques for analyzing efficiency, linearity, and linearization in a 5G active antenna transmitter context,” *IEEE Microw. Mag.*, vol. 20, no. 5, pp. 35–49, May2019.
[4] H.Holma, A.Toskala, and T.Nakamura, *5G Technology: 3GPP New Radio*. Hoboken, NJ, USA: Wiley, 2019.
[5] S. C.Cripps, “A theory for the prediction of GaAs FET load-pull power contours,” in *IEEE MTT-S Int. Microw. Symp. Dig.*, May 1983, pp. 221–223.
[6] J. C.Pedro, L. C.Nunes, and P. M.Cabral, “A simple method to estimate the output power and efficiency load–pull contours of class-B power amplifiers,” *IEEE Trans. Microw. Theory Techn.*, vol. 63, no. 4, pp. 1239–1249, Apr.2015.
[7] D. P.Nguyen, J.Curtis, and A.-V.Pham, “A Doherty amplifier with modified load modulation scheme based on load–pull data,” *IEEE Trans. Microw. Theory Techn.*, vol. 66, no. 1, pp. 227–236, Jan.2018.
[8] D.Nopchindaand K.Buisman, “Measurement technique to emulate signal coupling between power amplifiers,” *IEEE Trans. Microw. Theory Techn.*, vol. 66, no. 4, pp. 2034–2046, Apr.2018.
[9] W.Hallberg, D.Nopchinda, C.Fager, and K.Buisman, “Emulation of Doherty amplifiers using single-amplifier load–pull measurements,” *IEEE Microw. Wireless Compon. Lett.*, vol. 30, no. 1, pp. 47–49, Jan.2020.
[10] M.Mengozzi et al., “Experimental validation of a system-level model for active arrays under emulated beam steering,” *IEEE Microw. Wireless Technol. Lett.*, vol. 35, no. 11, pp. 1–4, Nov.2025.
[11] D.Nopchinda, T.Eriksson, H.Zirath, and K.Buisman, “Measurement of reflection and transmission coefficients using finite impulse response least-squares estimation,” *IEEE Trans. Microw. Theory Techn.*, vol. 68, no. 1, pp. 222–235, Jan.2020.
[12] J.Fernandez et al., “Neural network based nonlinear forward model identification for digital MIMO arrays under load modulation,” in *IEEE MTT-S Int. Microw. Symp. Dig.*, Jun. 2025, pp. 356–359.
[13] J.Fernandez et al., “Over-the-air linearization of phased array transmitters affected by load modulation,” *IEEE Trans. Circuits Syst. I, Reg. Papers*, vol. 72, no. 5, pp. 2366–2379, May2025.
[14] *RF WebLab*. Accessed: Dec. 2025. [Online]. Available: http://dpdcompetition.com/rfweblab/
[15] J.Fernandez, L.Anttila, M.Valkama, and T.Eriksson, “Linearization of active array transmitters under crosstalk via over-the-air observations,” in *Proc. 31st Eur. Signal Process. Conf. (EUSIPCO)*, Sep. 2023, pp. 1420–1424.